Fabrication of visible-light active Fe_2O_3-GQDs/NF-TiO_2 composite film with highly enhanced photoelectrocatalytic performance

Qi Wang[a,b], Naxin Zhu[a,c], Enqin Liu[a], Chenlu Zhang[a], John C. Crittenden[b], Yi Zhang[a] and Yanqing Cong[a,*]

[a]*School of Environmental Science and Engineering, Zhejiang Gongshang University, Hangzhou 310018, China*

[b]*The Brook Byer Institute for Sustainable Systems and School of Civil and Environmental Engineering, Georgia Institute of Technology, Atlanta 30332, USA*

[c]*Laboratory for Advanced Materials, Research Institute of Industrial Catalysis, East China University of Science and Technology, Shanghai 200237, China*

Abstract: Visible-light active Fe_2O_3-GQDs/NF-TiO_2 composite films were fabricated via sequential electro-deposition and electro-oxidation processes. The prepared photocatalytic films were extensively characterized using scanning electron microscopy (SEM), high-resolution transmission electron microscopy (HRTEM), X-ray diffraction (XRD), Raman spectroscopy and X-ray photoelectron spectroscopy (XPS). The results revealed that graphene quantum dots (GQDs) and α-Fe_2O_3 particles were simultaneously deposited onto the surface of N and F co-doped TiO_2 (NF-TiO_2) simply using a graphite sheet instead of a Pt sheet as anode in the electro-deposition process. The NF-TiO_2 substrate obtained by calcining TiO_2 nanotubes (TiO_2-NTs) in the presence of NH_4F displayed pyramid shapes with dominant (101) facets. Linear sweep voltammetry (LSV), electrochemical impedance spectroscopy (EIS) and Mott-Schottky (M-S) plots indicated that the generation, separation and transfer of photogenerated charges were greatly enhanced on the novel composite. The photocurrent density of Fe_2O_3-GQDs/NF-TiO_2 was 4.2 times that on Fe_2O_3/TiO_2-NTs at 0.5 V *vs.* Ag/AgCl under visible light irradiation. For the photoelectrocatalytic (PEC) reduction of Cr(VI) using

* To whom correspondence should be addressed. yqcong@hotmail.com (Y. Cong) Tel.: +86-571-28008211; Fax: +86-571-28008215

Fe$_2$O$_3$-GQDs/NF-TiO$_2$ as photoanode with a Ti sheet as cathode, substantially enhanced activity was achieved due to the combined effect of visible-light-active components (α-Fe$_2$O$_3$ and NF-TiO$_2$) and excellent electron mediator (GQDs). The calculated reduction rate constant was 7 times that obtained on Fe$_2$O$_3$/TiO$_2$-NTs film. Furthermore, both the long-time photocurrent and cyclic PEC reduction of Cr(VI) indicated good stability of the composite film.

Keywords: Cr(VI) reduction; NF-TiO$_2$; α-Fe$_2$O$_3$; GQDs; photoelectrocatalytic

1. Introduction

In recent decades, semiconductor photocatalysis has been recognized as one of the most promising methods for environmental remediation [1,2]. Based on photocatalysis, an improved performance was observed in the photoelectrocatalytic (PEC) process after the introduction of bias voltage, which promoted the separation of photogenerated electron−hole pairs [3-8]. In addition, the immobilized photocatalytic films in the PEC process can be easily reused, which is critical for future practical applications. However, it is still a great challenge to develop highly efficient photocatalytic material that can utilize more solar energy.

As the most extensively studied photocatalyst, pure TiO$_2$ can absorb only UV light and cannot be directly excited by visible light, which accounts for up to approximately 43% of solar radiation. Lattice doping and surface modification have both been investigated to overcome this problem and have proven effective [1,9-11]. Nonmetal doping, such as N doping, is recognized as one of the most promising way to narrow the band gap and extend the response of TiO$_2$ into visible region [10,12]. However, the oxidative power of N-doped TiO$_2$ (N-TiO$_2$) under visible light is relatively low due to the formation of a mixed gap composed of N 2p and O 2p above the valence band (VB). For example, the degradation of formic acid, NH$_3$ or I$^-$ barely proceeded on N-TiO$_2$ [13,14]. Previously, we observed the vital role of fluorine in tuning the band structure of N-TiO$_2$ [15]. Co-doping of F could enhance the oxidative power of N-TiO$_2$ and shift the conduction band (CB) to a more positive position [16,17].

1   Surface modification with another narrow band-based semiconductor is also a suitable

2   option to improve the visible light activity of TiO_2 [18-20]. N-type hematite (α-Fe_2O_3, 2.2 eV)

3   is recognized as a promising candidate due to its high visible light absorption, rich abundance

4   and low cost [21-23]. Enhanced photocatalytic activity under visible light has been reported

5   when coupled with TiO_2 or N-TiO_2 [24-29]. Because the CB of α-Fe_2O_3 lies below the CB of

6   TiO_2 [27,28], only high-energy electrons of α-Fe_2O_3, which constitute a small fraction of

7   photogenerated electrons, can be transferred to the CB of TiO_2 [25,29]. Thus, raising the CB

8   of α-Fe_2O_3 or lowering the CB of TiO_2 may be beneficial for the electron transfer process.

9   Because the co-doping of N and F can lower the CB position of TiO_2 [15], the construction of

10   a α-Fe_2O_3/NF-TiO_2 composite should be a more suitable choice than α-Fe_2O_3/N-TiO_2 or

11   α-Fe_2O_3/TiO_2. Low-energy electrons on α-Fe_2O_3 can be more efficiently utilized in this

12   composite.

13   Moreover, carbon materials have shown excellent promoting effect in the electron

14   transfer process [30-34]. For example, carbon nanotube, carbon quantum dots, graphene and

15   graphene quantum dots (GQDs) were all members of carbon family [35-38]. Recently,

16   graphene quantum dots (GQDs) with a small size (< 20 nm) have drawn considerable

17   attention. GQDs are intriguing in terms of their ability to accept and transfer photogenerated

18   electrons due to pronounced quantum confinement and edge effects. Thus, the performance

19   of α-Fe_2O_3/NF-TiO_2 can be further enhanced after the proper introduction of GQDs.

20   Herein, we report the first study and fabrication of a Fe_2O_3-GQDs/NF-TiO_2 composite

21   film with the aim of achieving highly efficient electron generation, separation and transfer.

22   The NF-TiO_2 substrate with pyramid-shape and dominant (101) facets was first prepared by

23   calcining TiO_2 nanotubes (TiO_2-NTs) with the assistance of NH_4F. The most stable (101)

24   facets was reported to be more reductive than the star facets of (001) [39-41], where

25   photo-deposition of Pt and reduction of O_2 preferentially occurred [40,42]. Herein, (101)

26   facets acted as highly active electron reservoirs. α-Fe_2O_3 and GQDs were deposited onto the

27   surface of NF-TiO_2 via sequential electro-deposition and electro-oxidation processes (Scheme

28   1). GQDs can be simultaneously deposited onto the surface of α-Fe_2O_3/NF-TiO_2 simply

1   using a graphite sheet instead of a Pt sheet as anode in the electro-deposition process. The

2   generation, separation and transfer of photogenerated charges on the prepared film electrodes

3   were compared using linear sweep voltammetry (LSV), electrochemical impedance

4   spectroscopy (EIS) and Mott-Schottky (M-S) plots. Moreover, Cr(VI), a carcinogen and

5   mutagen was used as a model pollutant for capturing the cathode electrons, with coexisting

6   organic pollutants as hole scavengers. Due to the combined effect of visible-light-active

7   components (α-Fe_2O_3 and NF-TiO_2) and the excellent electron conductors (GQDs), a highly

8   enhanced PEC performance was demonstrated using Fe_2O_3-GQDs/NF-TiO_2 as photoanode

9   and a Ti sheet as cathode.

10

11   **2. Experimental**

12   *2.1. Preparation of the Fe_2O_3-GQDs/NF-TiO_2 film electrode*
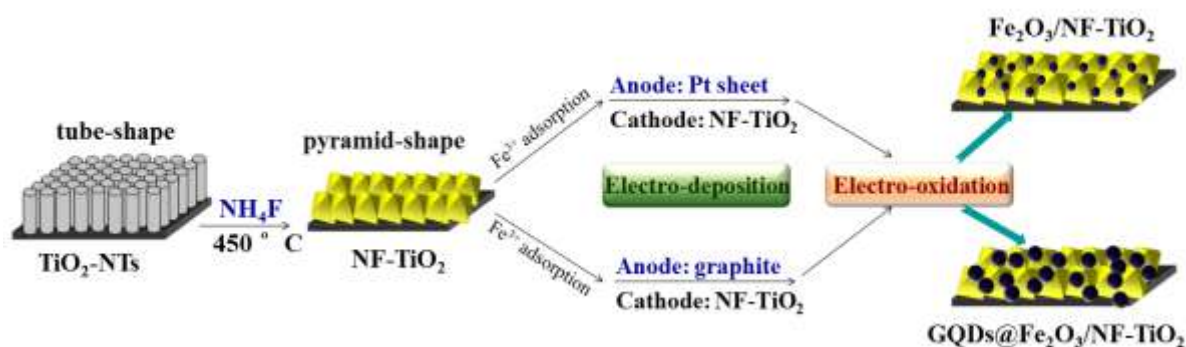
13

14   **Scheme 1.** Schematic depicting the preparation of Fe_2O_3/NF-TiO_2 and Fe_2O_3-GQDs/NF-TiO_2 films.

15   NF-TiO_2 film was obtained by calcining amorphous TiO_2-NTs film (prepared by a

16   traditional anodizing process [27,43]) in the presence of NH_4F at 450 °C for 2 h (Scheme 1).

17   TiO_2-NTs can be simultaneously etched and doped by HF and NH_3 originating from NH_4F

18   decomposition. As a control experiment, N-TiO_2 was also prepared using NH_4Cl instead of

19   NH_4F in the calcination process. The initial ratio of NH_4F to Ti substrate (cm^2) was maintained

20   at an optimal value of 0.2 g/cm^2.

21   Fe_2O_3-GQDs/NF-TiO_2 films were prepared via consecutive electro-deposition and

22   electro-oxidation processes (Scheme 1). Fe_2O_3/NF-TiO_2 was also prepared for comparison.

1   The two different films were fabricated using different anodes (Pt sheet or graphite) in the

2   electro-deposition process. For the deposition of Fe_2O_3, Fe^{3+} was first adsorbed onto the

3   surface of NF-TiO_2 by soaking the NF-TiO_2 film in $Fe(NO_3)_3$ aqueous solution (0.1 M) and

4   then converted to Fe^0 in the electro-deposition process. Finally, the electro-deposited Fe^0 was

5   transformed to Fe_2O_3 via anodization in a 1.0 M KOH aqueous solution for 2 min. As controls,

6   Fe_2O_3/TiO_2-NTs and Fe_2O_3/N-TiO_2 were also prepared in a manner similar to the

7   Fe_2O_3/NF-TiO_2 preparation process except that TiO_2-NTs or N-TiO_2 was used as the substrate

8   for Fe_2O_3 loading instead of NF-TiO_2.

9   *2.2. Characterization*

10   The morphology and structure of the prepared film samples were observed by a

11   scanning electron microscope (SEM, Hitachi S-4800, Tokyo, Japan) and a high-resolution

12   transmission electron microscope (HRTEM, JEOL JEM-2010, Tokyo, Japan). The chemical

13   state of component elements in the film samples was investigated by a VG Thermo Escalab

14   220i-XL X-ray photoelectron spectroscopy (XPS) with Al Kα at 1,486.6 eV. The binding

15   energies of Ti 2p, O 1s, C 1s, Fe 2p, N 1s and F 1s were referenced against C 1s (284.6 eV).

16   The crystal phases were detected by X-ray diffractometry (XRD) using a Bruke Regaku

17   D/Max-2500. The vibration modes were detected by Raman spectra which were recorded on

18   a thermo scientific DXR with exciting wavelength of 633 nm. The diffuse reflectance

19   UV-Vis absorption was recorded on a Hitachi U-3010 spectrophotometer. The photo-response

20   of the prepared films was tested under chopped light irradiation (500 W Xe lamp, Shanghai

21   lansheng) by an electrochemical station (CHI 660E). EIS analysis and M-S plots were also

22   measured in a three-electrode configuration by a CHI 660E electrochemical station.

23   *2.3. PEC study*

24   Unless otherwise noted, the PEC activities of the prepared film electrodes (anode) were

25   compared via the PEC reduction of Cr(VI) (80 μM) with Na_2SO_4 (0.2 mol/L) as the

26   electrolyte and 1 mM EDTA as a hole scavenger. A constant DC potential of 2.0 V was

27   applied to the photoanode with a Ti sheet as the cathode. The photoanode was irradiated by

1 visible light ($\lambda > 420$ nm, ca. 80 mW cm^{-2}) emitted from a halogen lamp (CEL-IW500,

2 Beijing Teach Jinyuan Technology Co., Ltd.) fitted with a cut-off filter and surrounded by a

3 cooling water jacket. Before turning on the light, the electrode was immersed in Cr(VI)

4 solution for 30 min to achieve adsorption-desorption equilibrium. Typically, the initial

5 solution pH was adjusted to 3.0. The concentration of Cr(VI) at different time intervals was

6 measured using the 1,5-diphenylcarbazide colorimetric method [44,45] on a UV-Vis

7 spectrophotometer (UV-2102PC, Unico Instruments Co., Ltd.). The purple complex of Cr(VI)

8 540 nm after adding chromogenic agent was barely affected by coexisting EDTA (Fig. S1).

9 Meanwhile, pH variations as a function of PEC reaction time were also monitored (Fig. S2).

10 In addition, the concentrations of coexisting organics, including EDTA (1.0 mM), phenol (10

11 mg/L), and methylene blue (MB, 10 μM) during the PEC process were also monitored. The

12 colorless phenol and EDTA were detected by HPLC, whereas the MB dye was monitored by

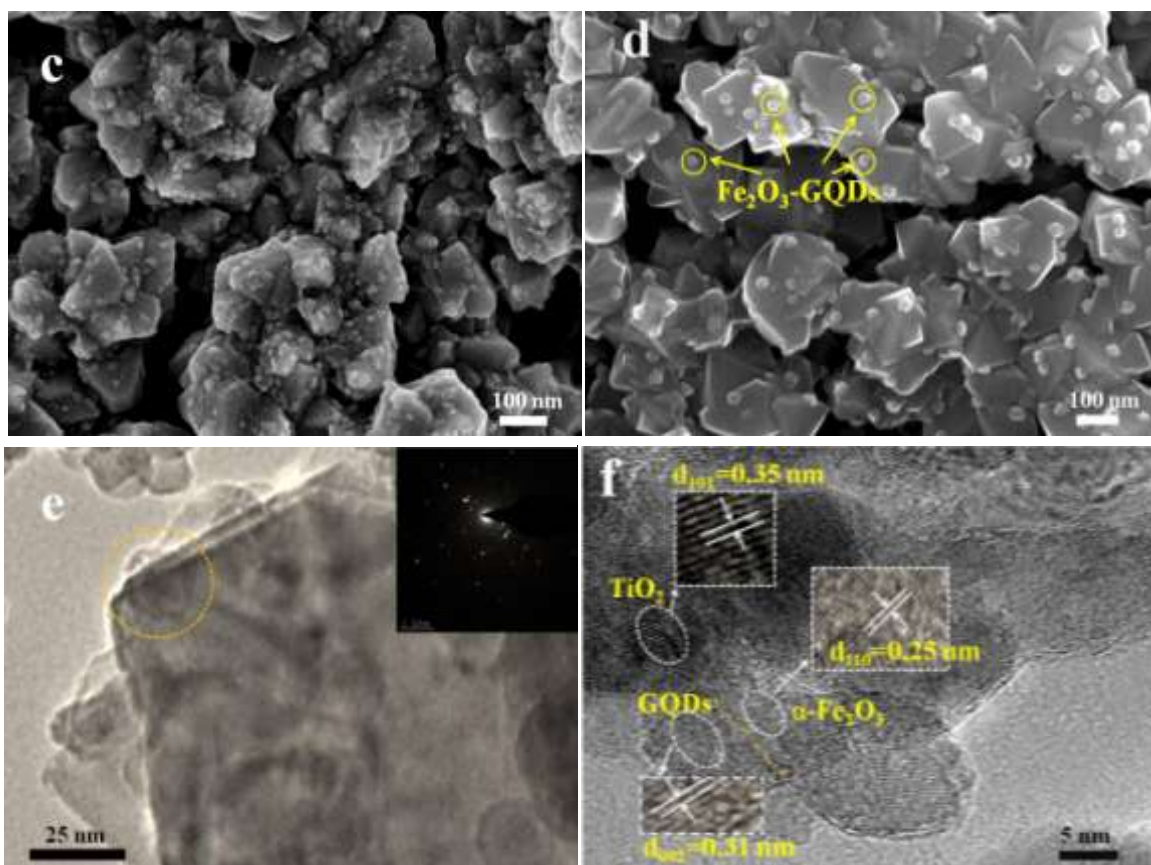13 its maximum absorption at 664 nm on a UV-Vis spectrophotometer.

14

15 **3. Results and discussion**

16 *3.1 SEM and HRTEM*

17
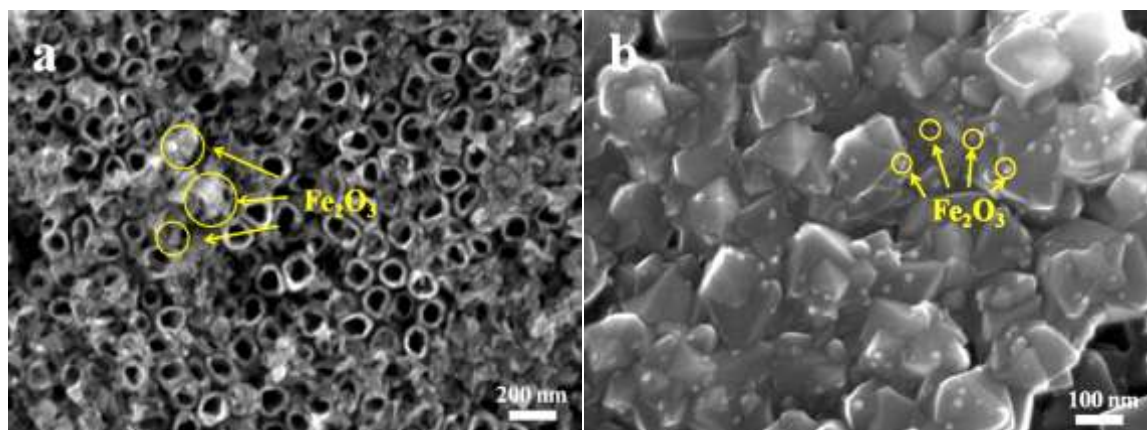
Fig. 1. SEM images of (a) Fe_2O_3/TiO_2-NTs, (b) Fe_2O_3/NF-TiO_2, (c) Fe_2O_3-GQDs/NF-TiO_2 (intermediate state) and (d) Fe_2O_3-GQDs/NF-TiO_2; (e) TEM and (f) HRTEM images of Fe_2O_3-GQDs/NF-TiO_2.

The prepared film electrodes were first characterized by SEM to investigate possible morphology changes. As shown in Fig. 1a, the Fe_2O_3/TiO_2-NTs surface was composed of TiO_2 nanotubes and Fe_2O_3 particles. Pyramid-shaped NF-TiO_2 was observed after calcining the TiO_2-NTs substrate in the presence of NH_4F (Fig. 1b). A control experiment using pure Ti foil instead of TiO_2-NTs was also performed to understand this interesting phenomenon. No pyramid-shaped structures were observed under identical calcination conditions (Fig. S3a). Moreover, a TiO_2-NTs surface was also calcined in the presence of NH_4Cl. The use of NH_4Cl instead of NH_4F led to the formation of particle-shaped products (Fig. S3b). In brief, the use of tubular structures as precursors and NH_4F as the additive were both essential for the formation of pyramid-shaped NF-TiO_2.

For Fe_2O_3/NF-TiO_2, smaller Fe_2O_3 particles (10-15 nm) were more uniformly deposited and dispersed on the surface of NF-TiO_2 (Fig. 1b). Interestingly, using different anodes (Pt

1 sheet or a graphite sheet) during the electro-deposition process will lead to the formation of

2 different Fe_2O_3-loaded electrodes (Fe_2O_3/NF-TiO_2 and Fe_2O_3-GQDs/NF-TiO_2). For example,

3 as shown in Scheme 1, when a graphite sheet is used as the anode for the electro-deposition

4 of Fe nanoparticles, graphite will be exfoliated simultaneously (Fig. S4) and will cover the

5 surface of NF-TiO_2. As shown in Fig. 1c, the intermediate state was captured when the next

6 oxidation step was not performed. The surface of NF-TiO_2 and deposited Fe^0 nanoparticles

7 was clearly covered by graphite-originated material. When this intermediate state was further

8 electrochemically oxidized in 1.0 mol/L KOH aqueous solution, Fe^0 was converted to Fe_2O_3

9 and the graphite-originated cover disappeared, leaving a clean NF-TiO_2 surface. However,

10 the particle size loaded onto NF-TiO_2 (Fig. 1d) was observed to be considerably larger than

11 that on Fe_2O_3/NF-TiO_2 using Pt as anode in the electro-deposition process. High-resolution

12 TEM (HRTEM) was performed to obtain more detailed structural information. Fig. 1e

13 illustrates that particles with a diameter of approximately 18 nm were loaded on the

14 pyramid-shaped substrate. The HRTEM image of the selected area is presented in Fig. 1f.

15 After fast Fourier transform (FFT), the lattice fringes of TiO_2, α-Fe_2O_3 and GQDs can all be

16 identified. For example, the lattice fringe spacing of 0.31 nm corresponds to the lattice

17 fringes of (002) planes of GQDs [46,47], whereas the values of 0.25 and 0.35 nm were

18 ascribed to the (110) plane of α-Fe_2O_3 [48] and the (101) plane of anatase TiO_2, respectively.

19 *3.2 XRD and Raman spectra*

20

8
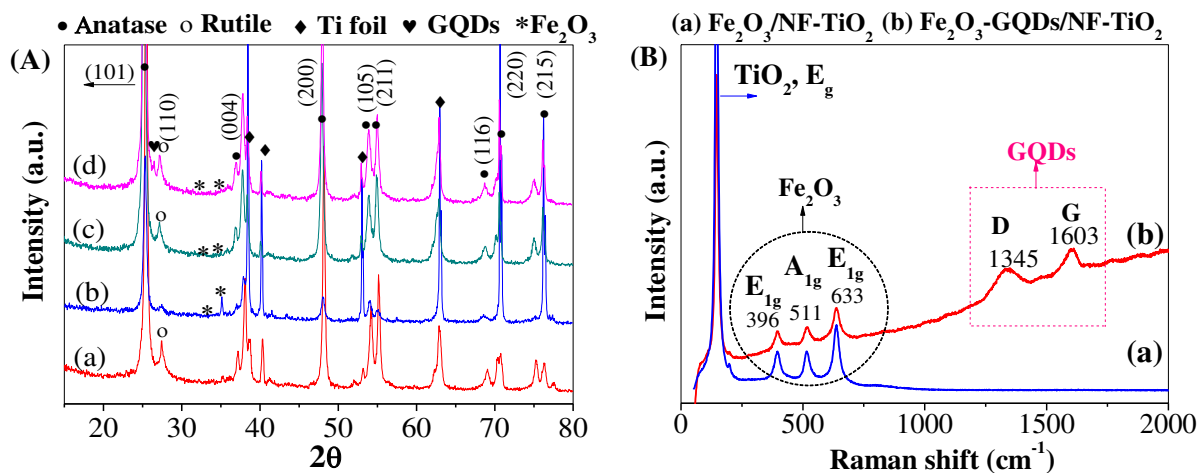
Fig. 2. (A) XRD patterns of NF-TiO$_2$ (a), Fe$_2$O$_3$/TiO$_2$-NTs (b), Fe$_2$O$_3$/NF-TiO$_2$ (c) and Fe$_2$O$_3$-GQDs/NF-TiO$_2$ (d); (B) Raman spectra of Fe$_2$O$_3$/NF-TiO$_2$ (a) and Fe$_2$O$_3$-GQDs/NF-TiO$_2$ (b).

XRD patterns of the prepared film electrodes were investigated, and the results are shown in Fig. 2A. The diffraction peaks at 25.3°, 37.9°, 48.1°, 54.0°, 55.1°, 68.8°, 70.3° and 75.1° correspond to (101), (004), (200), (105), (211), (116), (220) and (215) planes of anatase TiO$_2$, respectively. Distinct Rutile (110) signal can be observed in NF-TiO$_2$ (curve a). The presence of a small fraction of rutile may be beneficial for electron–hole separation under irradiation due to the formation of heterojunction. As for Fe$_2$O$_3$/TiO$_2$-NTs (curve b), pure anatase TiO$_2$ and distinct signals of the Ti substrate were observed. The characteristic diffraction peaks corresponding to α-Fe$_2$O$_3$ (JCPDS No. 33-0664) can also be observed [22]. However, very weak α-Fe$_2$O$_3$ signals can be observed in either Fe$_2$O$_3$/NF-TiO$_2$ or Fe$_2$O$_3$-GQDs/NF-TiO$_2$, which is probably due to the relatively small amount. Furthermore, Raman spectrum was carried out to confirm the presence of Fe$_2$O$_3$. As shown in Fig. 2B, typical A$_{1g}$ and E$_{1g}$ Raman modes of α-Fe$_2$O$_3$ [26] can be observed in both Fe$_2$O$_3$/NF-TiO$_2$ and Fe$_2$O$_3$-GQDs/NF-TiO$_2$.

Compared to Fe$_2$O$_3$/NF-TiO$_2$, a weak signal at 26.4° can be observed on Fe$_2$O$_3$-GQDs/NF-TiO$_2$ (Fig. S5), which is different from the characteristic and sharp diffraction peaks of either raw graphite (26.5°) [49] or expanded graphite (26.6°) [50]. Recently, Parvez et al. reported the electrochemical exfoliation of graphite into a graphene sheet, where the exfoliated products displayed a characteristic XRD peak at 26.3° [51]. The electrodeposition process (Scheme 1) in the present study is highly similar to Parvez's procedure, where graphite and Na$_2$SO$_4$ (which exhibited a pronounced exfoliation efficiency) were used as the anode and electrolyte, respectively. In addition to electro-deposition, subsequent electro-oxidation was added in the present study, which may destroy the sheet structure of graphene, leading to the small particle-shaped GQDs. The sp2 configuration of GQDs was further verified by Raman spectrum. As shown in Fig. 2B, distinct peaks of the D band (1345 cm^{-1}) and G band (1603 cm^{-1}) of graphene [52] can be observed on Fe$_2$O$_3$-GQDs/NF-TiO$_2$, whereas no such peaks appeared on Fe$_2$O$_3$/NF-TiO$_2$. These results

illustrate that GQDs were simultaneously formed and deposited together with Fe_2O_3 onto the surface of NF-TiO$_2$.

3.3 XPS

The chemical composition of Fe_2O_3-GQDs/NF-TiO$_2$ was further revealed by XPS spectra. As shown in Fig. 3A, signals of Ti 2p, O 1s, C 1s, Fe 2p, N 1s and F 1s can be observed. The N 1s and F 1s spectra, displayed in the insert of Fig. 3A, indicated the presence of O-Ti-N [53] and Ti-F species [54]. The high-resolution spectrum of C 1s (Fig. 3B) revealed the presence of C=C (284.4 eV), C–C (284.8 eV), C–O (285.4 eV) and O–C= O (288.2 eV) species [55]. As for Fe 2p (Fig. 3C), the two peaks at 711.2 eV and 724.8 eV were ascribed to Fe 2p$_{1/2}$ and Fe 2p$_{3/2}$, respectively. The distance between Fe 2p$_{1/2}$ and Fe 2p$_{3/2}$ is 13.6 eV, corresponding to Fe^{3+} in α-Fe_2O_3 [56,57]. An approximately 0.8 eV positive shift in the binding energy of Fe 2p can be observed in Fe_2O_3-GQDs/NF-TiO$_2$ relative to that in Fe_2O_3/NF-TiO$_2$. However, a negligible shift was observed for Ti 2p (Fig. 3D). Therefore, the presence of GQDs appears to play a vital role in affecting the electronic environment around the Fe atoms. Because it has been verified by HRTEM (Fig. 1d) that the GQDs and Fe_2O_3 nanoparticles were in contact with each other, the sp2 configuration of C=C bonds in GQDs will aid in the dispersion of electron density from Fe atoms to GQDs. Thus, the electron density around Fe_2O_3 will decrease, resulting in a higher binding energy [58]. In summary, it is reasonable to speculate that the electronic state of Fe_2O_3 is considerably different due to being covered by GQDs, which leads to the formation of Fe_2O_3-GQDs loaded onto pyramid-shaped NF-TiO$_2$.
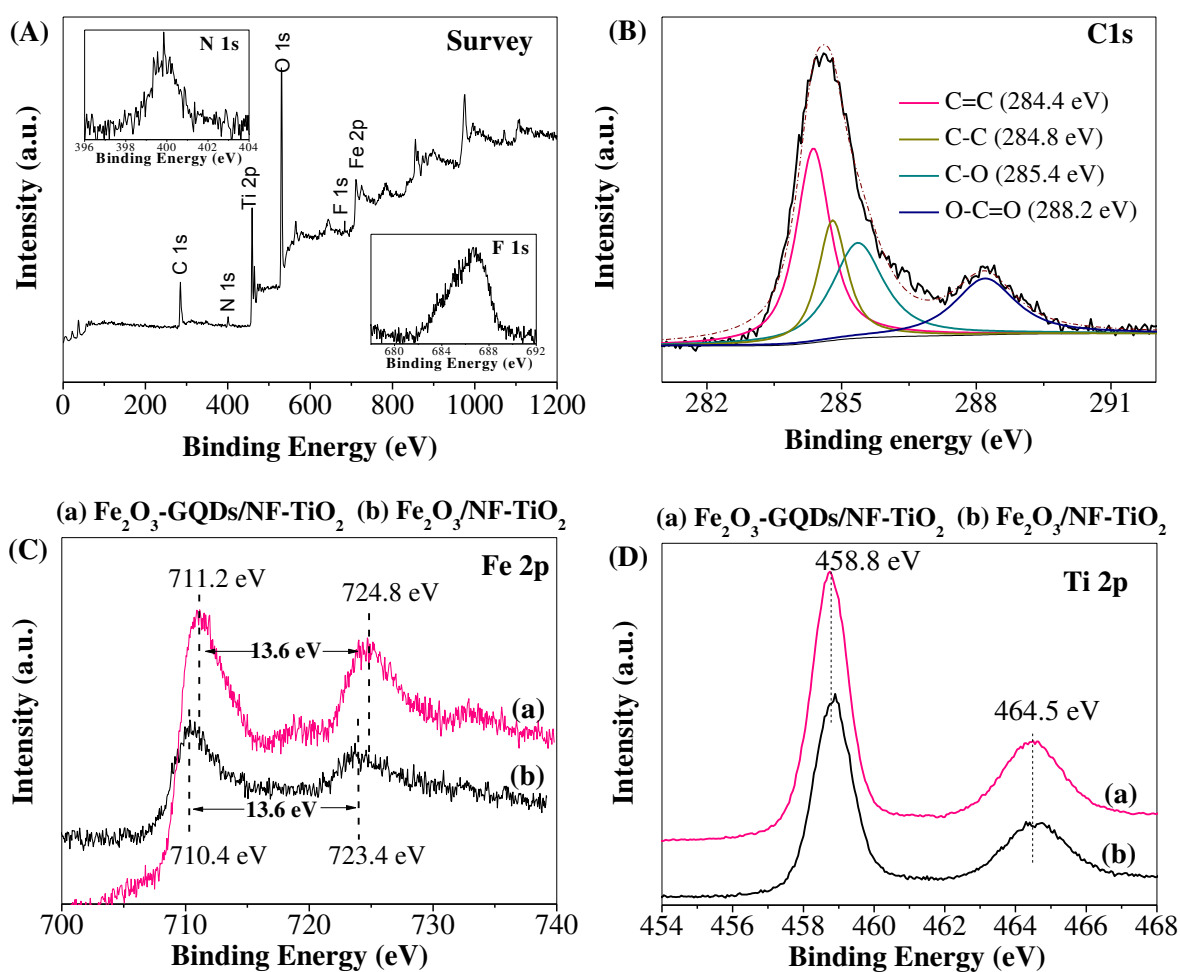
Fig. 3. (A) XPS survey spectrum taken from the surface of Fe_2O_3-GQDs/NF-TiO_2, insert: XPS spectra of N 1s and F 1s; (B) High-resolution XPS spectra of C 1s region; (C) Fe 2p and (D) Ti 2p region for Fe_2O_3-GQDs/NF-TiO_2 and Fe_2O_3/NF-TiO_2.

3.4 Electrochemical characterizations
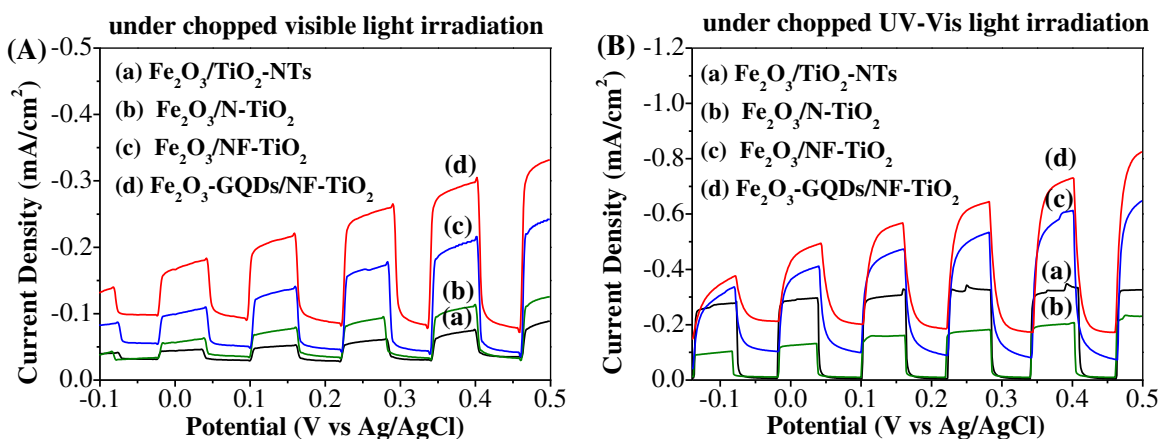
Fig. 4. Photocurrent response of different films under the irradiation of (A) chopped visible light ($\lambda > 420$

2 nm) and (B) chopped UV-Vis light.

3   The photocurrent response of the prepared films was tested and compared in 0.1 M

4 Na_2SO_4 and Na_2SO_3 mixed aqueous solution under both chopped visible light ($\lambda > 420$ nm)

5 and UV-Vis light irradiation. As illustrated in Fig. 4, the Fe_2O_3-GQDs/NF-TiO_2 film exhibited

6 the highest current density. Interestingly, large dark currents were always observed on

7 NF-TiO_2 based samples. For more accurate comparison of the photocurrent density among

8 different photoanodes, the dark currents were deducted and the results were shown in Fig. S6.

9 Under visible light irradiation (Fig. S6A), the photocurrent density was -0.252 mA/cm^{-2} at 0.5

10 V *vs.* Ag/AgCl on Fe_2O_3-GQDs/NF-TiO_2, which was approximately 4.2 times that of

11 Fe_2O_3/TiO_2-NTs (-0.059 mA/cm^{-2}). Compared to pristine TiO_2-NTs, which cannot be excited

12 by visible light, a greatly enhanced current density was also observed on Fe_2O_3/TiO_2-NTs

13 (Fig. S7), indicating that Fe_2O_3 acts as a visible light sensitizer. In addition, although the

14 Fe_2O_3/NF-TiO_2 film (Fig. 4A, curve c) was prepared by a similar process as the

15 Fe_2O_3-GQDs/NF-TiO_2 film, a greatly enhanced photocurrent response was observed on the

16 latter one. The difference was ascribed to the introduction of GQDs, which may be beneficial

17 for electron transfer. Moreover, the onset potential of different photoanodes were also

18 compared (Fig. S8) [59,60]. It showed that more negative onset potential and increased

19 photocurrent density can be observed on Fe_2O_3-GQDs/NF-TiO_2 film electrode.
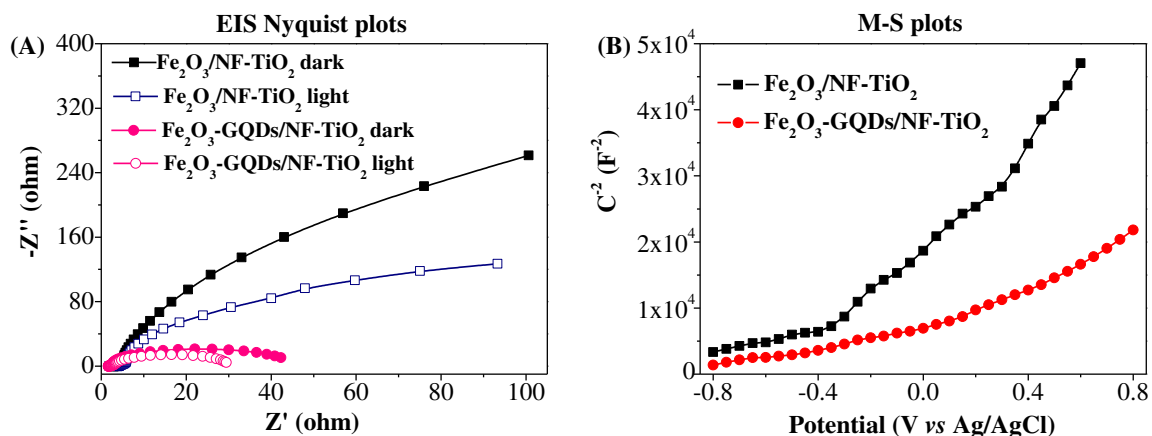
20

21 **Fig. 5.** (A) EIS Nyquist plots measured in 0.5 M Na_2SO_4 aqueous solution with a frequency range of 100

1 kHz to 0.01 Hz and a scan rate of 5 mV s^{-1}; (B) M-S plots of different film electrodes measured in 0.2 M

2 Na_2SO_4 at 500 Hz.

3   EIS measurements were performed as EIS Nyquist plots can provide useful information

4 on the electron-transfer process across the electrode-electrolyte interface. The EIS Nyquist

5 plots of the different film electrodes were compared and the results were presented in Fig. S9.

6 It can be observed that Fe_2O_3-GQDs/NF-TiO$_2$ exhibited smallest circular radius both in the

7 dark and under visible light irradiation. Since small circular radius typically indicates a lower

8 charge transfer resistance [61], lowest charge transfer resistance can be deduced on

9 Fe_2O_3-GQDs/NF-TiO$_2$. In order to clarify the role of GQDs, The EIS Nyquist plots of

10 Fe_2O_3/NF-TiO$_2$ and Fe_2O_3-GQDs/NF-TiO$_2$ were also compared. As shown in Fig. 5A, the

11 introducing of GQDs can greatly reduce charge transfer resistance.

12   In addition to EIS analysis, M-S plots under dark conditions were also investigated to

13 compare the charge carrier density of different film electrodes. The carrier density can be

14 deduced from the slopes of the M-S plots using the following equation [62]:

15
$$C_{SC}^{-2} = \frac{2}{\varepsilon_0 \varepsilon e N_D}(E - E_{fb} - \frac{kT}{e}) \qquad (1)$$

16 where C_{SC} is the space-charge layer capacitance, N_D is the dopant density, ε_0 is the vacuum

17 permittivity, ε is the relative dielectric constant of the oxide film, k is the Boltzmann constant,

18 T is the temperature and kT/e is a negligibly small correction term. As illustrated in Fig. 5B,

19 the slope observed on Fe_2O_3-GQDs/NF-TiO$_2$ was much smaller after the introducing of

20 GQDs, indicating higher carrier density. Thus, Fe_2O_3-GQDs/NF-TiO$_2$ is highly likely to

21 achieve a better PEC performance when it is used for the removal of pollutants due to the

22 easier generation and transfer of electron-hole pairs.

23   Overall, easier generation, more efficient separation and enhanced transfer efficiency of

24 photogenerated electron-hole pairs can be achieved on an Fe_2O_3-GQDs/NF-TiO$_2$ due to the

25 combined effect of the visible-light-active components (Fe_2O_3 and NF-TiO$_2$) and the

26 excellent electron mediator (GQDs). Therefore, the utilization of the superior

27 photoelectrochemical properties for PEC applications in environmental remediation should

1   be further investigated.

2   *3.5. PEC activity*

3   Hexavalent chromium (Cr(VI)) is toxic, carcinogenic and highly mobile in water and soil.

4   Every year, a tremendous amount of wastewater containing Cr(VI) is discharged from

5   industrial processes, such as electroplating, leather tanning, wood preservation and pigment

6   use [15,44]. Thus, the detoxification of Cr(VI) is of vital importance. Cr(VI) is typically

7   reduced to nontoxic Cr(III), which can be removed from aqueous solutions in the form of

8    $Cr(OH)_3$. Compared to traditional processes for Cr(VI) reduction, photocatalytic and PEC

9   methods are efficient and environmentally friendly, which can avoid secondary pollution [63].

10   In the present study, Cr(VI) was selected as a model pollutant. The prepared film samples were

11   tested as photoanode with a Ti sheet as cathode for the reduction of Cr(VI) under visible light.

12   As shown in Fig. 6A, Fe_2O_3-GQDs/NF-TiO_2 exhibited the highest PEC activity among the

13   tested photoanodes. The estimated rate constant (k: 0.0231 min) (Fig. 6B) was 7 times that of

14   Fe_2O_3/TiO_2-NTs (k: 0.0033 min^{-1}). Since GQDs were reported to enhance the PEC activity of

15   TiO_2 [35,36], control experiment using GQDs/NF-TiO_2 as photoanode was also carried out in

16   the present study. As shown in Fig. 6B, about 4 times rate constant enhancement can still be

17   observed on Fe_2O_3-GQDs/NF-TiO_2 relative to GQDs/NF-TiO_2 (k: 0.0062 min^{-1}). Thus, the

18   co-loading of Fe_2O_3 and GQDs are very important. Besides, pH of the solutions before,

19   during and after photocatalytic reaction were also measured and the results were presented in

20   Fig. S2. It can be observed that pH of the solutions gradually increased from 3.0 to 3.5.

21   The optimal Fe_2O_3-GQDs/NF-TiO_2 film was further tested in single photocatalytic (PC)

22   or electrocatalytic (EC) processes to confirm the superiority of the PEC process. As shown in

23   Figs. 6C-D, a synergistic effect can be observed in the PEC process, and the synergistic factor

24   (*SF*) was calculated to be 2.9 according to the following equation [64]:

$$SF = \frac{k_{PEC}}{k_{PEC} + k_{EC}} \qquad (2)$$

25   where k_{PEC}, k_{PC} and k_{EC} represent rate constants for Cr(VI) reduction in the PEC, PC and EC

1 processes, respectively.
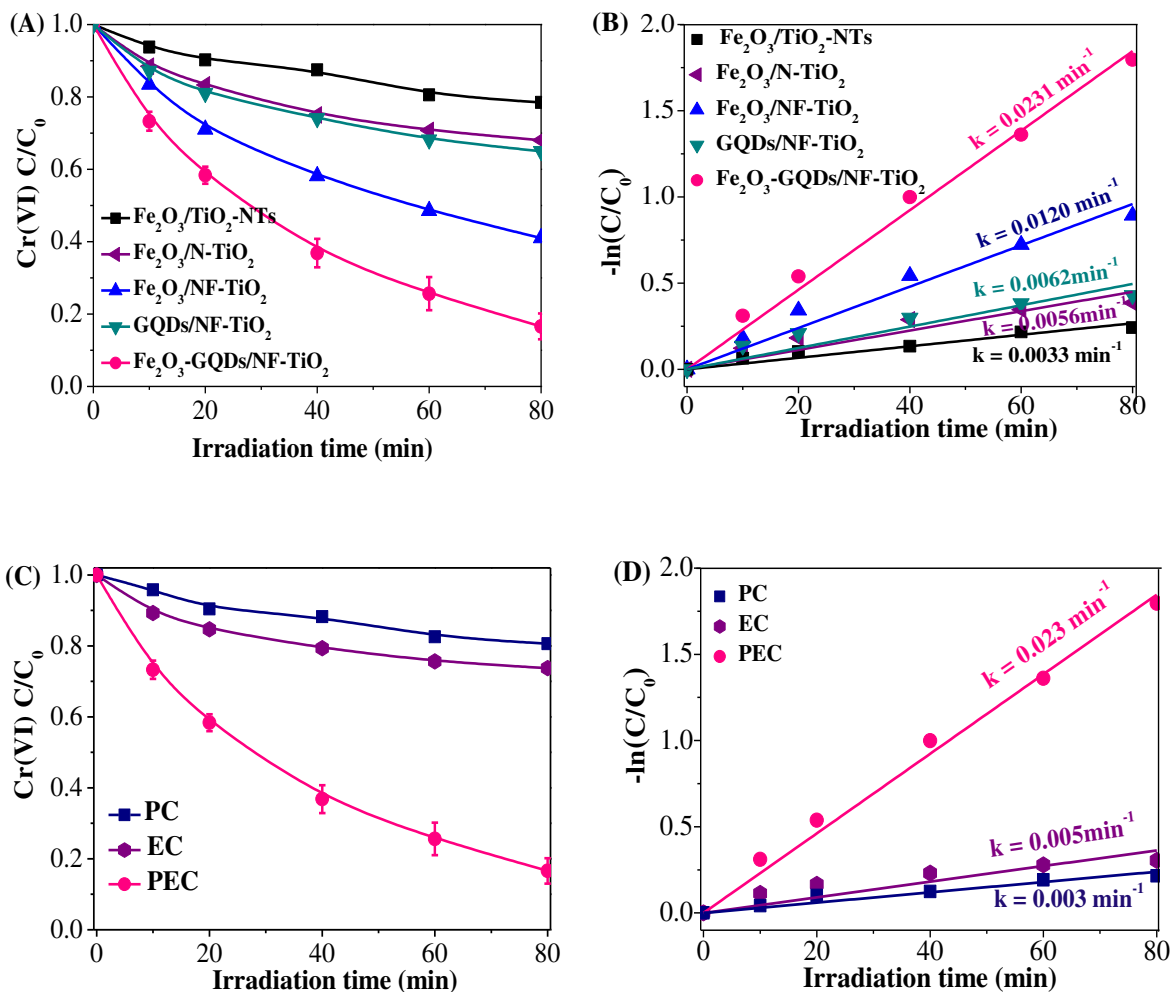
Fig. 6. (A) PEC reduction dynamics and (B) pseudo-first-order kinetic curves of Cr(VI) using different photoanodes; (C) Comparison of Cr(VI) reduction dynamics and (D) pseudo-first-order kinetic curves using Fe$_2$O$_3$-GQDs/NF-TiO$_2$ electrode under different processes. Reaction conditions: 2.0 V, 0.2 M Na$_2$SO$_4$, pH 3.0, 80 μM Cr(VI), 1 mM EDTA.

Because the photocatalytic performance of Fe$_2$O$_3$-GQDs/NF-TiO$_2$ can be markedly increased with the assistance of applied potential, the effect of different applied potentials was investigated, and the results are presented in Fig. 7. The PEC reduction of Cr(VI) was easier at a higher applied potential within the range of 1.0 V to 3.0 V. Moreover, the efficiency of electrochemical enhancement (*E*, in *%*) was estimated.

$$E = \left(\frac{k_{PEC} - k_{PC}}{k_{PEC}}\right) \times 100\% \qquad (3)$$

According to the above equation [65], the E value at 1.0 V was calculated to be 45.6%, whereas it increases considerably to 87.0% at 2.0 V. However, the enhancement trend slowed down, with an E value of 93.6%, when the applied potential further increased to 3.0 V. Thus, 2.0 V was selected for the following study for the purpose of energy conservation.
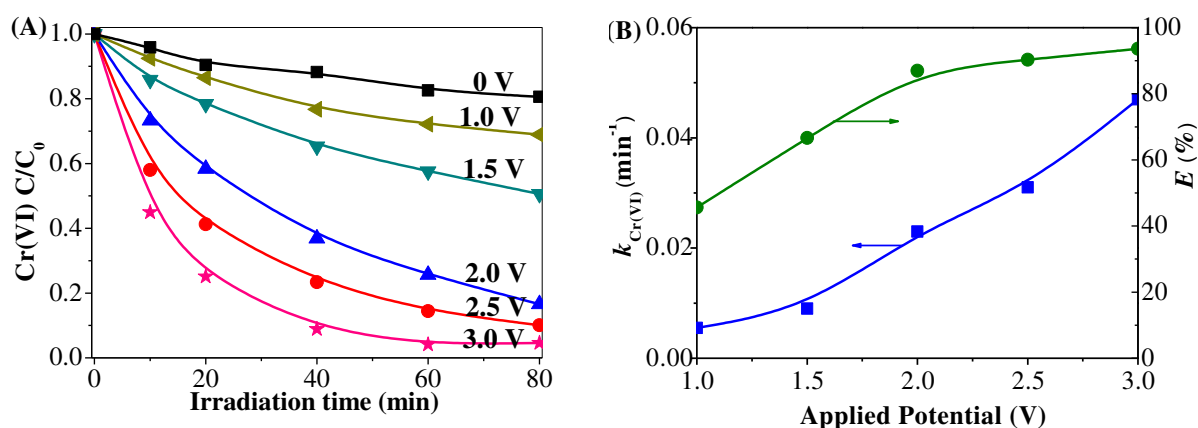

Fig. 7. Effect of external potential on the PEC reduction of Cr(VI) on Fe_2O_3-GQDs/NF-TiO_2 under visible light irradiation (A) reduction dynamics, (B) estimated rate constants and $E\%$. Reaction conditions: 2.0 V, 0.2 M Na_2SO_4, pH 3.0, 80 μM Cr(VI), 1 mM EDTA.

A large amount of organic pollutants are also observed in Cr(VI)-containing wastewater. For example, EDTA has been detected as a common chelating agent, which may arise from various industrial processes and form metal-EDTA complexes [4-7,66-68]. Thus, in addition to metal ions reduction, the degradation of co-existing organic pollutants was also of vital importance. As illustrated in Figs. 8A and Fig. S10, the simultaneous PEC reduction of Cr(VI) and degradation of EDTA can be observed in the present system. Moreover, the reduction of Cr(VI) was greatly improved by the presence of EDTA. With an increasing EDTA concentration (Fig. 8B), the removal efficiency of Cr(VI) increased from 40% to 91% after 80 min of the PEC reaction. Meanwhile, the presence of other organics was also investigated. As shown in Fig. S11, the presence of either colorless phenol or colored MB dye can greatly promote the reduction of Cr(VI). The organics themselves were also degraded simultaneously.

16

1 Thus, the Fe$_2$O$_3$-GQDs/NF-TiO$_2$ composite electrode was suitable for handling

2 Cr(VI)-organic co-polluted wastewater.
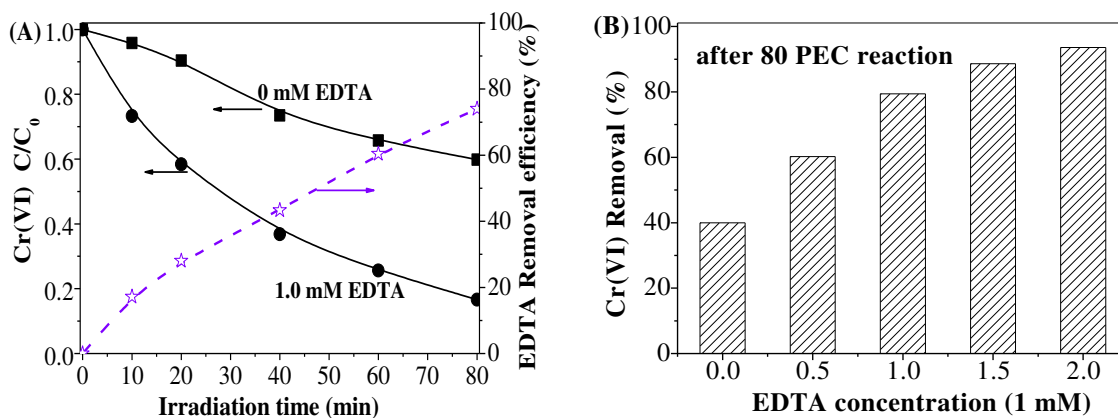
3

4 **Fig. 8.** (A) Effect of EDTA concentration on the PEC reduction of Cr(VI) (left) and simultaneous removal

5 efficiency of 1.0 mM EDTA (right) using a Fe$_2$O$_3$-GQDs/NF-TiO$_2$ electrode. (B) Relationship between

6 Cr(VI) removal efficiency and coexisting EDTA concentration. External potential: 2.0 V. Electrolyte: 0.2

7 M Na$_2$SO$_4$, pH = 3.0.
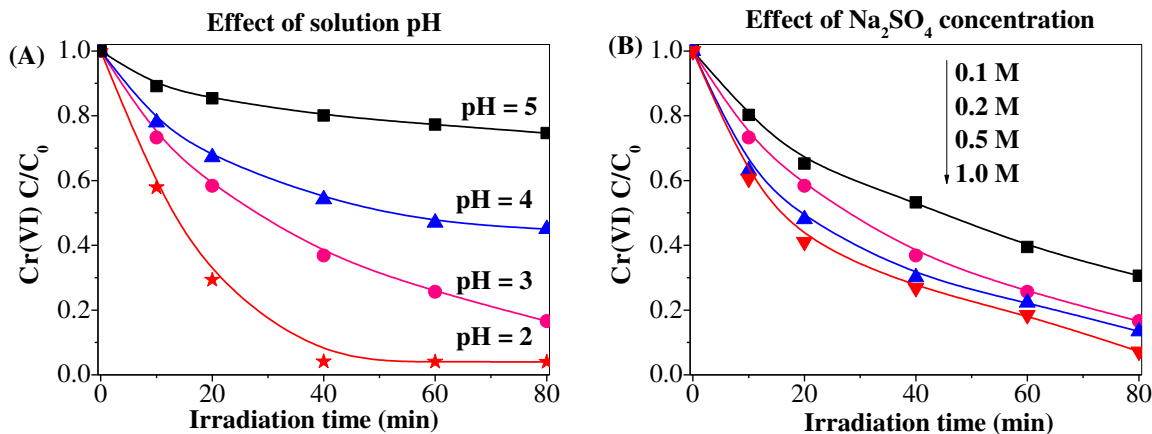

8

9 **Fig. 9.** (A) Influence of solution pH and (B) electrolyte concentration on the PEC reduction of Cr(VI).

10 Reaction conditions: Fe$_2$O$_3$-GQDs/NF-TiO$_2$, 80 μM Cr(VI), 1 mM EDTA.

11 Experiments with different initial solution pH were also performed, as pH has always

12 been considered an important factor for Cr(VI) reduction. As shown in Fig. 9A, the reduction

13 of Cr(VI) is easier to carry out under lower pH. The reason may be as follows: (1) The

14 Cr(VI)/Cr(III) redox potential became larger at low pH due to the different predominant

17

1   states of Cr(VI) (E^0(CrO$_4^{2-}$/Cr(OH)$_3$) = -0.13 V *vs.* NHE, E^0(HCrO$_4^-$/Cr^{3+}) = 1.35 V *vs.* NHE)

2   [69], which led to an increased thermodynamic driving force for Cr(VI) reduction; (2) The

3   VB edge of the photoanode shifted along with the CB edge to a more positive position at

4   lower pH, which led to increased oxidative ability for EDTA degradation [64] and

5   subsequently more efficient electron-hole separation.

6   In the present study, the PEC experiments were performed using Na$_2$SO$_4$ as an

7   electrolyte to increase conductivity. Thus, the concentration of Na$_2$SO$_4$ may also affect the

8   PEC activity for Cr(VI) reduction [70]. As shown in Fig. 9B, the reduction of Cr(VI) was

9   enhanced by increasing the Na$_2$SO$_4$ concentration. In addition, the enhancement trend slowed

10   down when the Na$_2$SO$_4$ concentration was further increased to 1.0 M. In general, the above

11   results indicate that the prepared photoanode is suitable for handling high-salinity

12   wastewater.

13   *3.6 Stability of the Fe$_2$O$_3$-GQDs/NF-TiO$_2$ electrode*
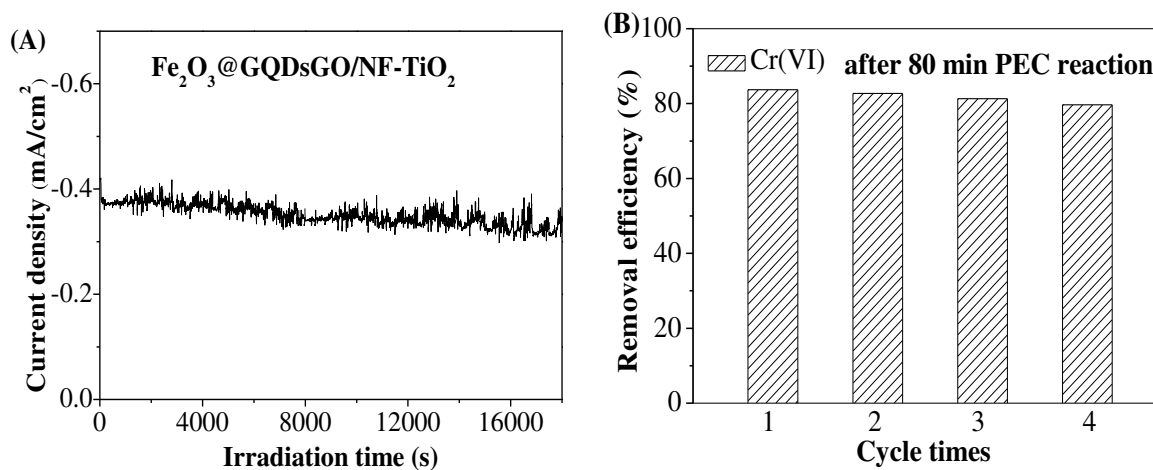

14

15   **Fig. 10** (A) Long-time photocurrent decay curve measured under visible light irradiation at a constant

16   potential of 0.5 V (*vs.* Ag/AgCl) for Fe$_2$O$_3$-GQDs/NF-TiO$_2$ film in 0.1 M Na$_2$SO$_4$ and Na$_2$SO$_3$ mixed

17   aqueous solution; (B) Cyclic removal of both Cr(VI) and phenol using the Fe$_2$O$_3$-GQDs/NF-TiO$_2$

18   photoanode under visible light irradiation.

19   As an excellent photocatalytic electrode, the stability of the PEC performance is critical.

1   In the present study, the Fe_2O_3-GQDs/NF-TiO_2 film was evaluated via both a long-time

2   photocurrent test and cyclic PEC experiments for Cr(VI) reduction. As shown in Fig. 10A,

3   the photocurrent generated on the Fe_2O_3-GQDs/NF-TiO_2 film was extremely stable and

4   exhibited nearly no attenuation within 18,000 s (5 h) of constant visible light irradiation. The

5   optimized film electrode was also tested in 4 successive cyclic PEC runs, and the results are

6   presented in Fig. 10B. The removal efficiencies were relatively consistent over 4 cycles.

7   Overall, the Fe_2O_3-GQDs/NF-TiO_2 film electrode exhibited superior PEC performance and

8   stability.

9   *3.7. Proposed mechanism*
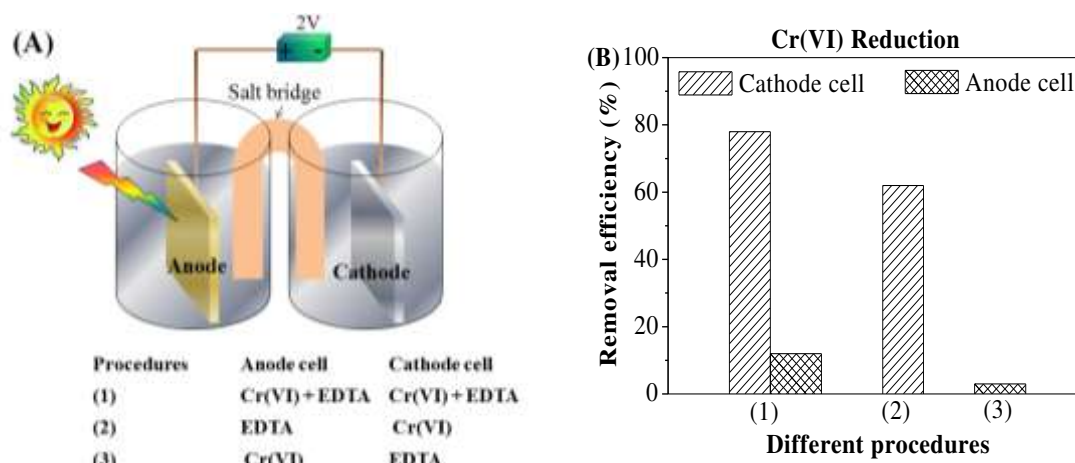
11   **Fig. 11.** (A) Schematic illustration of experiments using a salt bridge and (B) Cr(VI) removal efficiencies

12   in different PEC processes. Reaction conditions: 2.0 V, 0.2 M Na_2SO_4, pH 3.0, 80 μM Cr(VI), 1 mM

13   EDTA.

14   In the present study, the visible-light-active Fe_2O_3-GQDs/NF-TiO_2 film was applied as

15   anode with a Ti sheet as cathode, respectively. The photogenerated electrons on the

16   photoanode are anticipated to be driven to the cathode with the assistance of applied positive

17   potential. In this manner, the photogenerated holes left on the anode and electrons on the

18   cathode will lead to subsequent oxidation and reduction reactions, respectively. Experiments

19   using salt bridges were performed to verify this assumption (Fig. 11A). The PEC reduction of

20   Cr(VI) was performed using two separate glass cells under different conditions, and the

1   results are shown in Fig. 11B. It can be observed that Cr(VI) was predominately reduced in

2   the cathode cell.

3   Based on all the above results and analyses, tentative mechanisms for the reduction of

4   Cr(VI) and the separation/transfer of photogenerated electron-hole pairs on

5   Fe_2O_3-GQDs/NF-TiO_2 are presented in Scheme 2. For NF-TiO_2, both anatase and rutile

6   phases were identified by XRD analysis. Due to the different band gaps and CB positions

7   [71-73], the intrinsic band difference between anatase and rutile TiO_2 will be beneficial for

8   electron–hole separation. In addition, although α-Fe_2O_3 was reported to possess a lower

9   independent CB position relative to TiO_2, the same Fermi level tended to be achieved

10   between α-Fe_2O_3 and NF-TiO_2 when they were in contact with each other. In this manner, the

11   CB of α-Fe_2O_3 would move to a more negative position [29]. XPS analysis (Fig. 3C) has

12   shown that the introduction of GQDs will lead to the dispersion of electron density from the

13   Fe atoms to the GQDs. Herein, the GQDs act as an electron accelerator, which will be

14   beneficial for the process of electron transfer from Fe_2O_3 to TiO_2. Finally, the separated

15   electrons will be driven to the cathode by an applied positive potential, and the holes will be

16   kept on the photoanode. Thus, an efficient separation of photogenerated electron-hole pairs

17   will be achieved due to the synergistic effect among Fe_2O_3, GQDs and NF-TiO_2.
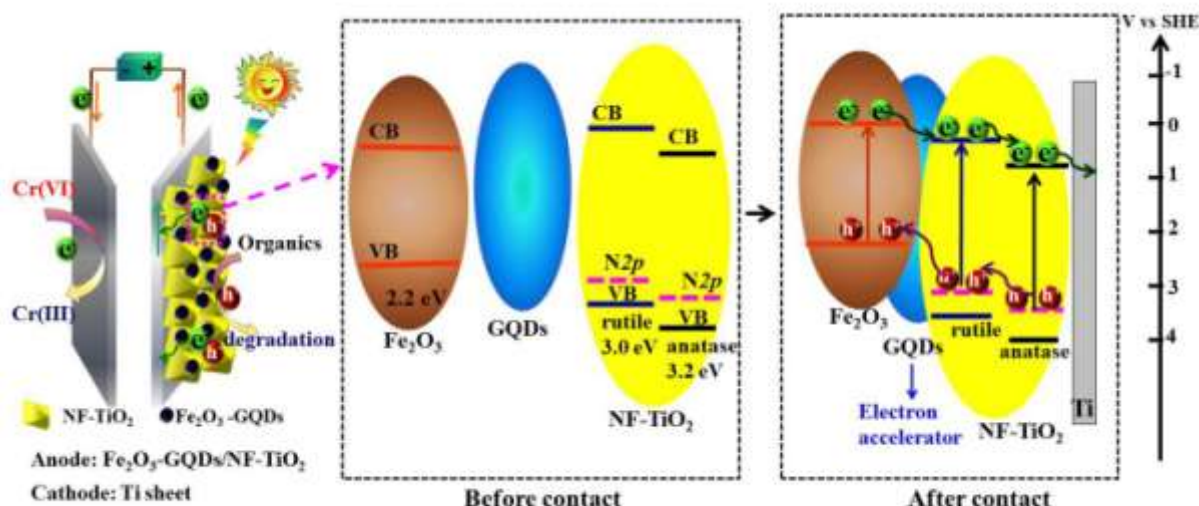
18

19   **Scheme 2.** Schematic illustration for the PEC reduction of Cr(VI) (left) and the separation/transfer of

20   photogenerated electron–hole pairs on Fe_2O_3-GQDs/NF-TiO_2 during the PEC process (right).

4. Conclusion

In the present study, a visible-light active Fe_2O_3-GQDs/NF-TiO_2 composite film was fabricated by simultaneously loading α-Fe_2O_3 and GQDs onto pyramid-shaped NF-TiO_2. NH_4F plays a vital role in transforming tubular TiO_2-NTs into pyramid-shaped NF-TiO_2 with dominant (101) facets. Easier generation, separation and transfer of e^--h^+ pairs was facilitated due to the combined effect of visible-light active components (α-Fe_2O_3 and NF-TiO_2) and excellent electron accelerators (GQDs). For example, electrochemical characterizations indicated that the visible-light-induced photocurrent density at 0.4 V vs. Ag/AgCl was approximately 4 times that on Fe_2O_3/TiO_2-NTs. Superior PEC activity for Cr(VI) reduction and stability were observed when using Fe_2O_3-GQDs/NF-TiO_2 as anode with a Ti sheet as cathode. The pseudo first-order rate constant $k_{Cr(VI)}$ increased by 7 times relative to that on Fe_2O_3/TiO_2-NTs. Furthermore, the selected photoanode also exhibited good stability in the long-time photocurrent test and reuse processes for Cr(VI) reduction. Overall, the present study developed a promising film electrode for environmental application, particularly for treating Cr(VI)-organic co-polluted wastewater.

References

[1] C.C. Chen, W.H. Ma, J.C. Zhao, Chem. Soc. Rev. 39 (2010) 4206–4219.

[2] Y.Y. Zhu, Y.J. Wang, Q. Ling, Y.F. Zhu, Appl. Catal. B Environ. 200 (2017) 222–229.

[3] D. Wang, X. Li, J. Chen, X. Tao, Chem. Eng. J. 198-199 (2012) 547–554.

[4] H. Zeng, S. Liu, B. Chai, D. Cao, Y. Wang, X. Zhao, Environ. Sci. Technol. 50 (2016) 6459–6466.

[5] X. Zhao, L. Guo, J. Qu, Chem. Eng. J. 239 (2014) 53–59.

[6] X. Zhao, L. Guo, B. Zhang, H. Liu, J. Qu, Environ. Sci. Technol. 47 (2013) 4480–4488.

[7] X. Zhao, J. Zhang, J. Qu, Electrochimica Acta 180 (2015) 129–137.

[8] S.N. Chai, G.H. Zhao, Y.N. Zhang, Y.J. Wang, F.Q. Nong, M.F. Li, D.M. Li, Environ. Sci. Technol. 46 (2012) 10182–10190.

[9] W.J. Jiang, M. Zhang, J. Wang, Y.F Liu, Y.F Zhu, Appl. Catal. B: Environ. 160–161 (2014) 44–50.

[10]H.B. Fu, L.W. Zhang, S.C. Zhang, Y.F. Zhu, J.C. Zhao, J. Phys. Chem. B 110 (2006) 3061–3065.

[11]S.M. Zhou, D.K. Ma, P. Cai, W. Chen, S.M. Huang, Mater. Res. Bull. 60 (2014) 64–71.

[12]R. Asahi, T. Morikawa, T. Ohwaki, K. Aoki, Y. Taga, Science 293 (2001) 269–271.

[13]M. Mrowetz, W. Balcerski, A. J. Colussi, M. R. Hoffmann, J. Phys. Chem. B 108 (2004) 17269–17273.

[14]R. Nakamura, T. Tanaka, Y. Nakato, J. Phys. Chem. B 108 (2004) 10617–10620.

[15]Q. Wang, C.C. Chen, W.H. Ma, H.Y. Zhu, J.C. Zhao, Chem. Eur. J. 15 (2009) 4765–4769.

[16]L. Di, H. Hajime, H. Shunichi, O. Naoki, Chem. Mater. 17 (2005) 2596–2602.

[17]J. Andersen, C. Han, K. O'Shea, D.D. Dionysiou, Appl. Catal. B: Environ. 154–155 (2014) 259–266.

[18]J. Zhu, S.H. Wang, J.G. Wang, D.Q. Zhang, H.X. Li, Appl. Catal. B: Environ. 102 (2011) 120–125.

[19]M. Pelaez, N.T. Nolan, S.C. Pillai, M.K. Seery, P. Falarasd, A.G. Kontos, P.S.M. Dunlop, J.W.J. Hamilton, J.A. Byrne, K. O'Shea, M.H. Entezari, D.D. Dionysiou, Appl. Catal. B: Environ. 125 (2012) 331–349.

[20]Y. Wang, Y. Zhang, G.H. Zhao, H. Tian, H. Shi, T. Zhou, ACS Appl. Mater. Inter. 4 (2012) 3965–3972.

[21]M. Forster, R.J. Potter, Y. Ling, Y. Yang, D.R. Klug, Y. Lid, A.J. Cowan, Chem. Sci. 6 (2015) 4009–4016.

[22]D. Xiao, K. Dai, Y. Qu, Y. Yin, H. Chen, Appl. Surf. Sci. 358 (2015) 181–187.

[23] P. Cai, S. M. Zhou, D.K. Ma, S.N. Liu, W. Chen, S.M. Huang, Nano-Micro Lett. 7 (2015) 183–193.

[24] W. Hung, T. Chien, C. Tseng, J. Phys. Chem. C 118 (2014) 12676–12681.

[25] X. Li, H. Lin, X. Chen, H. Niu, J. Liu, T. Zhang, F. Qu, Phys. Chem. Chem. Phys. 18 (2016) 9176–9185.

[26] J. Liu, S. Yang, W. Wu, Q. Tian, S. Cui, Z. Dai, F. Ren, X. Xiao, C. Jiang, ACS Sustainable Chem. Eng. 3 (2015) 2975–2984.

[27] Y.Q. Cong, Z. Li, Y. Zhang, Q. Wang, Q. Xu, Chem. Eng. J. 191 (2012) 356–363.

[28] S.Y. Kuang, L.X. Yang, S.L. Luo, Q.Y. Cai, Appl. Surf. Sci. 255 (2009) 7385–7388.

[29] P. Luan, Mi. Xie, D. Liu, X. Fu, L. Jing, Sci. Rep. 4 (2014) 6180

[30] N. Gao, X. Fang, Chem. Rev. 115 (2015) 8294–8343.

[31] X.J. Bai, L. Wang, Y.J. Wang, W.Q. Yao, Y.F. Zhu, Appl. Catal. B: Environ. 152–153 (2014) 262–270.

[32] Y.B. Wang, H.Y. Zhao, G.H. Zhao, Appl. Catal. B: Environ. 164 (2015) 396–406.

[33] H.Y. Zhao, Y.J. Wang, Y.B. Wang, T.C. Cao, G.H. Zhao, Appl. Catal. B: Environ. 125 (2012) 120–127.

[34] Y.J. Wang, G.H. Zhao, S.N. Chai, H.Y. Zhao, Y.B. Wang, ACS Appl. Mater. Inter. 5 (2013) 842–852.

[35] Y. N. Zhang, H. Y. Tian, G. H. Zhao, ChemElectroChem 2 (2015) 1728–1734.

[36] Y. Q. Zhang, D. K. Ma, Y. G. Zhang, W. Chen, S. M. Huang, Nano Energy 2 (2013) 545–552.

[37] Y.W. Zeng, D.K. Ma, W. Wang, J.J. Chen, L. Zhou, Y.Z. Zheng, K. Yu, S.M. Huang, Appl. Surf. Sci. 342 (2015) 136–143.

[38] Y.Q. Zhang, D.K. Ma, Y. Zhuang, X. Zhang, W. Chen, L.L. Hong, Q.X. Yan, K. Yu, S.M. Huang, J. Mate. Chem. 22 (2012) 16714–16718.

[39] Z. Xiong, X.S. Zhao, J. Am. Chem. Soc. 134 (2012) 5754–5757.

[40] T.R. Gordon, M. Cargnello, T. Paik, F. Mangolini, R.T. Weber, P. Fornasiero, C.B. Murray, J. Am. Chem. Soc. 134 (2012) 6751–6761.

[41] J. Pan, G. Liu, G.Q. Lu, H. Cheng, Angew. Chem. Int. Ed. 123 (2011) 2181–2185.

[42] T. Tachikawa, S. Yamashita, T. Majima, J. Am. Chem. Soc. 133 (2011) 7197–7204.

[43] Y.Q. Cong, Z. Li, Q. Wang, Y. Zhang, Q. Xu, F.X. Fu, Acta Phys.‑Chim. Sin. 28 (2012) 1489–1496.

[44] Q. Wang, X. Chen, K. Yu, Y. Zhang, Y. Cong, J. Hazard. Mater. 246–247 (2013) 135–144.

[45] A. Idris, N. Hassan, R. Rashid, A.F. Ngomsik, J. Hazard. Mater. 186 (2011) 629–635.

[46] J. Ge, M. Lan, B. Zhou, W. Liu, L. Guo, H. Wang, Q. Jia, G. Niu, X. Huang, H. Zhou, X. Meng, P. Wang, C.S. Lee, W. Zhang, X. Han, Nat. Comm. 5 (2014) 4596.

[47] Y. Dong, H. Pang, H. Yang, C. Guo, J. Shao, Y. Chi, C. Li, T. Yu, Angew. Chem. Int. Ed. 52 (2013) 7800–7804.

[48] S. Chen, Y. Xin, Y. Zhou, F. Zhang, Y. Ma, H. Zhou, L. Qi, J. Mater. Chem. A 3 (2015) 13377–13383.

[49] X. Lv, X. Xue, G. Jiang, D. Wu, T. Sheng, H. Zhou, X. Xu, J. Colloid Interf. Sci. 417 (2014) 51–59.

[50] X. Yu, Y. Zhang, X. Cheng, Electrochim. Acta 137 (2014) 668–675.

[51] K. Parvez, Z. Wu, R. Li, X. Liu, R. Graf, X. Feng, K. Müllen, J. Am. Chem. Soc. 136 (2014) 6083–6091.

[52] R. Liu, D. Wu, X. Feng, K. Müllen, J. Am. Chem. Soc. 133 (2011) 15221–15223.

[53] G. Liu, H. Yang, X. Wang, L. Cheng, J. Pan, G. Lu, H. Cheng, J. Am. Chem. Soc. 131 (2009) 12868–12869.

[54] J. Pan, G. Liu, G.Q. Lu, H. Cheng, Angew. Chem. Int. Ed. 123 (2011) 2181–2185.

[55] Y. Li, Y. Hu, Y. Zhao, G. Shi, L. Deng, Y. Hou, L. Qu, Adv. Mater. 23 (2011) 776–780.

[56] Y.Q. Cong, M.M. Chen, T. Xu, Y. Zhang, Q. Wang, Appl. Catal. B: Environ. 147 (2014) 733–740.

[57] A. Kleiman-Shwarsctein, A.J.F. Y.-S. Hu, G.D. Stucky, E.W. McFarland, J. Phy. Chem. C 112 (2008) 15900–15907.

[58] M. Sathish, B. Viswanathan, R.P. Viswanath, C.S. Gopinath, Chem. Mater. 17 (2005)

6349–6353.

[59] H.J. Shi, G.H. Zhao, J. Phys. Chem. C 118 (2014) 25939–25946.

[60] N. Mirbagheri, D. Wang, C. Peng, J. Wang, Q. Huang, C. Fan, E.E. Ferapontova, ACS Catal. 4 (2014) 2006–2015.

[61] A.J. Bard, L.R. Faulker, JohnWiley & Sons: New York, (2001) 386.

[62] H. Chen, G. Liu, L. Wang, Sci Rep. 5 (2015) 10852.

[63] Y. Li, W.Q. Cui, L. Liu, R.L. Zong, W. Yao, Y.H. Liang, Y.F. Zhu, Appl. Catal. B: Environ. 199 (2016) 412–423.

[64] Q. Wang, X.D. Shi, E.Q. Liu, J.J. Xu, J.C. Crittenden, Y. Zhang, Y.Q. Cong, Ind. Eng. Chem. Res. 55 (2016) 4897–4904.

[65] S. Garcia-Segura, S. Dosta, J.M. Guilemany, E. Brillas, Appl. Catal. B: Environ. 132–133 (2013) 142–150.

[66] G. Kim, W. Choi, Appl. Catal. B: Environ. 100 (2010) 77–83.

[67] X. Zhao, L. Guo, C. Hu, H. Liu, J. Qu, Appl. Catal. B: Environ. 144 (2014) 478–485.

[68] H. Zeng, S. Tian, H. Liu, B. Chai, X. Zhao, Chem. Eng. J. 301 (2016) 371–379.

[69] Q. Wang, X.D. Shi, E.Q. Liu, J.C. Crittenden, X.J. Ma, Y. Zhang, Y.Q. Cong, J. Hazard. Mater. 317 (2016) 8–16.

[70] J. Chen, Y. Xia, Q. Dai, Electrochim. Acta 165 (2015) 277–287.

[71] Y. Nosaka, A.Y. Nosaka, J. Phys. Chem. Lett. 7 (2016) 431–434.

[72] M.G. Ju, G. Sun, J. Wang, Q. Meng, W.Z. Liang, ACS Appl. Mater. Inter. 6 (2014) 12885–12892.

[73] P. Deák, B. Aradi, T. Frauenheim, J. Phys. Chem. C 115 (2011) 344–346.

Graphical Abstract